Self-consistent electronic structure of a vortex line in a type-II superconductor

François Gygi* and Michael Schlüter
AT&T Bell Laboratories, 600 Mountain Avenue, Murray Hill, New Jersey 07974
(Received 30 November 1990)

The electronic structure of a vortex line in a type-II superconductor is calculated self-consistently in the framework of the Bogoliubov–de Gennes theory. The Debye frequency, the Fermi velocity, and the coupling constant of the electron-electron attractive interaction are used as microscopic input parameters. The resulting quasiparticle-excitation spectrum, the pair potential, and the current distribution are studied as a function of temperature, and can be used to define a coherence length and to determine the magnetic penetration depth. The local density of one-particle excitations, calculated from the quasiparticle amplitudes, explains the results of scanning-tunneling-microscopy (STM) experiments by Hess *et al.* [Phys. Rev. Lett. **62**, 214 (1989)] on $NbSe_2$. The main spectroscopic features in the experimental results are caused by bound states in the vortex cores. Spatial distortions of the bound-state wave functions caused by neighboring vortices and by the crystalline lattice are discussed in terms of a simplified two-band model. In the case of $NbSe_2$, the resulting local density of states has a characteristic star shape in real space, whose orientation is energy dependent, in agreement with recent STM experiments [Phys. Rev. Lett. **64**, 2711 (1990)].

I. INTRODUCTION

The determination of the electronic properties of vortex lines in type-II superconductors has been a problem of longstanding interest. The phenomenological Ginzburg-Landau theory[1] has been used extensively to describe the properties of either isolated flux lines or of an Abrikosov flux lattice,[2] and formed the basis for discussions of macroscopic equilibrium quantities in terms of the empirically determined coherence length ξ and magnetic penetration depth λ. Since the Ginzburg-Landau theory is strictly valid only at temperatures close to the critical temperature T_c, or when the magnetic field is close to the upper critical field H_{c2}, various modifications have been proposed in order to extend its validity, in particular in the dirty limit, or when the Ginzburg-Landau parameter $\kappa \equiv \lambda/\xi$ is large.[2] On the other hand, calculations based on the microscopic BCS-Gor'kov theory have been limited by the complexity of the Gor'kov equations for inhomogeneous systems. Eilenberger[3] managed to reduce this complexity by transforming the Gor'kov equations into first-order equations, at the price of integrating out the energy variable of the Green functions. Ground-state properties, such as the gap parameter $\Delta(\mathbf{r})$ and the vector potential $\mathbf{A}(\mathbf{r})$ can be determined from such energy-averaged Green functions. This method was used by Kramer and Pesch,[4] and later by Klein[5] to calculate numerically the structure of a vortex line at low temperatures. A different approach was followed by Caroli, de Gennes and Matricon[6] and later by Bardeen *et al.*,[7] who solved the Bogoliubov–de Gennes equations for a vortex line using various approximations. This procedure, which relies of the assumption that there exist well-defined quasiparticles in the superconductor, has the advantage of providing information about the one-particle excitations of the system. The quasiparticle excitation spectrum can be obtained, together with the corresponding quasiparticle amplitudes. The Bogoliubov–de Gennes formalism is essentially correct in the weak-coupling regime, but also yields qualitative results in situations of very strong coupling, as was pointed out by Bishop *et al.*[8] The interest in microscopic electronic structure calculations of this type was revived recently by low-temperature scanning-tunneling-microscopy (STM) experiments which provided extremely detailed, spatially resolved, excitation spectra of a type-II superconductor in the presence of an Abrikosov flux lattice. An explanation of these results requires the knowledge of the one-particle local density of states of the system, which is best described in the framework of the Bogoliubov–de Gennes theory.[9–11] In that spirit, Shore *et al.*[12] and Gygi and Schlüter[13] recently obtained numerical solutions for quasiparticle amplitudes in a vortex core starting with approximate forms for the pair potential. This allowed them to discuss the most important features of the solutions, i.e., the presence of strongly bound low-energy states, already mentioned by Caroli *et al.*[6] responsible for an enhanced local density of states at the Fermi level at the center of a vortex core. This enhancement explains anomalies observed in the scanning-tunneling-microscopy (STM) experiment by Hess *et al.*[14] on $NbSe_2$. It is important to note that, in these two calculations,[12,13] the pair potential used as input was modeled from the experimentally inferred coherence length. The effect of the spatial dependence of the magnetic field was neglected, which seemed to be justified by the fact that the Ginzburg-Landau parameter κ is large in $NbSe_2$. The self-consistency of the solutions so obtained could not be checked in either case; in Ref. 12 because scattering states were not included in the calculation, and in Ref. 13 because only the lowest angular momentum eigenstates were included. A fully self-consistent solution of the Bogoliubov–de Gennes equations is therefore desirable since it provides information

about the detailed structure of the pair potential and of the current and magnetic field distributions in a vortex line at any temperature, as well as the dependence of these quantities on microscopic parameters. This allows one to calculate without empirical parameters one-particle properties such as the local density of states, which can in turn be used to determine the tunneling conductance measured in an STM experiment.

In this paper, we present the first fully self-consistent electronic structure of an isolated vortex line in a type-II superconductor, calculated in the framework of the Bogoliubov–de Gennes theory. The solutions are obtained iteratively. First, the Bogoliubov–de Gennes equations are solved in the presence of a spatially varying model vector potential $\mathbf{A}(\mathbf{r})$ corresponding to a total magnetic flux of one flux quantum $\phi_0=\pi\hbar c/e$. The resulting quasiparticle amplitudes and excitation energies are then used to determine a new pair potential and a new current distribution. A new vector potential is determined from the current distribution by solving Maxwell's equation and the process is iterated until convergence is attained. All input parameters used in the calculation are microscopic parameters which can in principle be obtained from band structure calculations. These parameters are the Debye frequency ω_D, the Fermi velocity v_F, and the coupling constant g describing the electron-electron attractive interaction. After a self-consistent solution has been obtained, the coherence length ξ and the magnetic penetration depth λ can be defined, and their values can be determined from the spatial dependence of the self-consistent pair potential and of the current distribution.

In a further step, the interaction of a vortex line with the crystal potential is then investigated in more detail for the case of $NbSe_2$. An angular band structure is derived using a simple two-band model. The resulting local density of states[15] explains more recent STM results showing star-shaped patterns in the tunneling conductance images of a vortex line[16] in $NbSe_2$. Furthermore, the energy dependence of the spatial orientation of these stars is well accounted for by the simple model.

The rest of this paper is organized as follows. In Sec. II, we describe the method of calculation. Section III contains self-consistent numerical results computed at various temperatures for a superconductor comparable to $NbSe_2$. In Sec. IV, we discuss various perturbations that can distort a flux line and modify its excitation spectrum and density of states.

II. BOGOLIUBOV–de GENNES EQUATIONS FOR A VORTEX LINE

In the presence of a magnetic field, the Bogoliubov–de Gennes equations[10] for the quasiparticles amplitudes $u_i(\mathbf{r})$ and $v_i(\mathbf{r})$ read

$$\left[\frac{1}{2m}\left[\mathbf{p}-\frac{e}{c}\mathbf{A}(\mathbf{r})\right]^2+U(\mathbf{r})-E_F\right]u_i(\mathbf{r})+\Delta(\mathbf{r})v_i(\mathbf{r})=E_i u_i(\mathbf{r}) ,$$
$$-\left[\frac{1}{2m}\left[\mathbf{p}+\frac{e}{c}\mathbf{A}(\mathbf{r})\right]^2+U(\mathbf{r})-E_F\right]v_i(\mathbf{r})+\Delta^*(\mathbf{r})u_i(\mathbf{r})=E_i v_i(\mathbf{r}) , \tag{1}$$

where $U(\mathbf{r})$ is the one-particle crystal potential, $\Delta(\mathbf{r})$ is the pair potential, and $A(\mathbf{r})$ is the vector potential. The index i denotes all quantum numbers. The pair potential and the current density depend on the solutions of Eq. (1)

$$\Delta(\mathbf{r})=g\sum_{E_i\le\hbar\omega_D}u_i(\mathbf{r})v_i^*(\mathbf{r})[1-2f(E_i)] , \tag{2}$$

$$\mathbf{j}(\mathbf{r})=\frac{e\hbar}{2mi}\sum_i\left[f(E_i)u_i^*(\mathbf{r})\left[\nabla-\frac{ie}{\hbar c}\mathbf{A}(\mathbf{r})\right]u_i(\mathbf{r})+[1-f(E_i)]v_i(\mathbf{r})\times\left[\nabla-\frac{ie}{\hbar c}\mathbf{A}(\mathbf{r})\right]v_i^*(\mathbf{r})-\text{H.c.}\right] , \tag{3}$$

where g is the coupling constant describing the electron-electron attractive interaction, ω_D is the Debye frequency, and $f(E)$ is the Fermi distribution. The vector potential $\mathbf{A}(\mathbf{r})$ is related to the current distribution $\mathbf{j}(\mathbf{r})$ by Maxwell's equation

$$\nabla\times\nabla\times\mathbf{A}=\frac{4\pi}{c}\mathbf{j} . \tag{4}$$

A self-consistent solution of these equations is obtained by repeatedly solving Eq. (1) and calculating $\Delta(\mathbf{r})$ and $\mathbf{A}(\mathbf{r})$ using Eqs. (2), (3), and (4), and reinserting them into Eq. (1) until convergence is attained.

We consider now the case of a vortex line oriented along the z direction. We neglect details of the one-particle potential $U(\mathbf{r})$ in Eq. (1), but include part of its effect by using effective masses m_ρ and m_z in the kinetic energy of Eq. (1). The system is therefore invariant under all rotations about the z axis, so that the solutions of the Bogoliubov–de Gennes equations have a well-defined planar angular momentum. This, together with translational invariance in the z direction, allows us to write the quasiparticle amplitude as

$$u(\mathbf{r})=u_{n\mu k_z}(r)e^{i(\mu-1/2)\theta}e^{ik_z z} ,$$
$$v(\mathbf{r})=v_{n\mu k_z}(r)e^{i(\mu+1/2)\theta}e^{ik_z z} , \tag{5}$$

where n is a radial quantum number and μ is *half* and odd integer.[6] Following Bardeen *et al.*,[7] we chose the gauge in which $\Delta(\mathbf{r})=|\Delta(r)|e^{-i\theta}$. In this gauge, and because of cylindrical symmetry, the vector potential reduces to

$$\mathbf{A}(\mathbf{r})=A_\theta(r)\hat{\mathbf{e}}_\theta \ . \tag{6}$$

The Bogoliubov–de Gennes equations are solved separately in each subspace of fixed angular momentum μ and fixed k_z by projecting the radial functions $u_n(r)$ and $v_n(r)$ onto a set of Bessel functions normalized in a disc of radius R

$$\phi_{jm}(r)=\frac{\sqrt{2}}{RJ_{m+1}(\alpha_{jm})}J_m\left[\alpha_{jm}\frac{r}{R}\right], \quad j=1,\ldots,N \ ,$$

where $m=\mu\pm\frac{1}{2}$ and where the argument α_{jm} is the jth zero of $J_m(x)$. The quasiparticle amplitudes $u_n(r)$ and $v_n(r)$ are expanded in the basis functions $\phi_{j\mu-1/2}(r)$ and $\phi_{j\mu+1/2}(r)$, respectively,

$$\begin{aligned} u_n(r)&=\sum_j c_{nj}\phi_{j\mu-1/2}(r) \ , \\ v_n(r)&=\sum_j d_{nj}\phi_{j\mu+1/2}(r) \ . \end{aligned} \tag{7}$$

This reduces Eq. (1) to a $2N\times 2N$ matrix eigenvalue problem

$$\begin{bmatrix} T^- & \Delta \\ \Delta^T & T^+ \end{bmatrix}\Psi_n=E_n\Psi_n \ , \tag{8}$$

where $\Psi_n^T=(c_{n1},\ldots,c_{nN},d_{n1},\ldots,d_{nN})$. The matrix elements of the Hamiltonian are

$$\begin{aligned} T^{\pm}_{jj'}&=\left\langle j\mu\pm\frac{1}{2}\left|\pm\left[\frac{1}{2m^*}\left[\mathbf{p}\mp\frac{e}{c}\mathbf{A}\right]^2-E_F\right]\right|j'\mu\pm\frac{1}{2}\right\rangle \\ &=\frac{\hbar^2}{2m_\rho}\left\{\left[\frac{\alpha^2_{j\mu\pm1/2}}{R^2}+\left[\frac{m_\rho}{m_z}\right]k_z^2\right]\delta_{jj'}+(\mu\pm\tfrac{1}{2})\frac{2e}{\hbar c}\int\phi_{j\mu\pm1/2}(r)\frac{A_\theta(r)}{r}\phi_{j'\mu\pm1/2}(r)r\,dr\right. \\ &\quad\left.+\left[\frac{e}{\hbar c}\right]^2\int\phi_{j\mu\pm1/2}(r)A_\theta^2(r)\phi_{j'\mu\pm1/2}(r)r\,dr\right\}-E_F \end{aligned} \tag{9}$$

and

$$\begin{aligned} \Delta_{jj'}&=\langle j\mu-\tfrac{1}{2}|\Delta(\mathbf{r})|j'\mu+\tfrac{1}{2}\rangle \\ &=\int\phi_{j\mu-1/2}(r)|\Delta(r)|\phi_{j'\mu+1/2}(r)r\,dr \ . \end{aligned} \tag{10}$$

Solving the secular problem (8) yields a set of eigenvalues E_n and their associated eigenvectors Ψ_n. The positive eigenvalues are interpreted as the energies required to create excitations having an angular momentum μ.[7] Negative eigenvalues correspond to the destruction of excitations with angular momentum μ. The Bogoliubov–de Gennes equations are invariant under the transformation

$$u_i(\mathbf{r})\rightarrow v_i^*(\mathbf{r}), \quad v_i(\mathbf{r})\rightarrow -u_i^*(\mathbf{r}), \quad E_i\rightarrow -E_i \tag{11}$$

which relates an eigenstate to its time-reversed counterpart. In the case of the vortex line, this allows one to identify a *negative* energy excitation having angular momentum $+\mu$ with a *positive* energy excitation having angular momentum $-\mu$. This identification can be used to reduce the computational effort by solving Eq. (8) for positive values of μ only, and by using Eq. (11) to obtain the positive energy eigenstates for negative angular momenta.

In order to be able to discuss the results of STM experiments performed in the presence of vortex lines, we need a model of the tunneling current between the microscope tip and the surface of the sample. This current is related to the one-particle spectral functions in the tip of the microscope and in the superconductor.[17] The latter can be expressed in terms of the quasiparticle amplitudes

$$A_S(\mathbf{r},E)=2\pi\sum_i[u_i^2(\mathbf{r})\delta(E-E_i)+v_i^2(\mathbf{r})\delta(E+E_i)] \ . \tag{12}$$

we assume here that the presence of the surface does not affect the quasiparticle amplitudes of the superconductor, so that we can use the solutions of Eq. (1) in Eq. (12). We also assume the spectral function of the tip to be that of a simple metal

$$A_N(\mathbf{r},E)=2\pi\sum_k\delta(E-E_k) \ . \tag{13}$$

If the tip is small compared to flux core dimensions, and is centered at position $\mathbf{r}$, the tunneling current due to an applied voltage V is

$$I(\mathbf{r},V)\propto\int\frac{dE}{2\pi}A_S(\mathbf{r},E)A_N(\mathbf{r},E+eV) \ . \tag{14}$$

The tunneling conductance is then given by

$$\begin{aligned} \frac{\partial I(\mathbf{r},V)}{\partial V}\propto-\sum_i[&u_i^2(\mathbf{r})f'(E_i-eV) \\ &+v_i^2(\mathbf{r})f'(E_i+eV)] \ , \end{aligned} \tag{15}$$

where $f'(E)$ is the derivative of the Fermi distribution. The quantity, calculated from the quasiparticle amplitudes, will be discussed in the next section, and compared with experimental observations.

The microscopic parameters used in the calculations were chosen so as to closely reproduce the properties of a superconductor comparable to $NbSe_2$. The superconducting gap of $NbSe_2$ is $\Delta_0\simeq 1.1$ MeV.[14] The value of the

coherence length obtained from measurements of the upper critical field ranges from $\xi \simeq 150$ a.u. to $\xi \simeq 190$ a.u. (Ref. 18). The magnetic penetration depth is $\lambda \simeq 1200$ a.u. and the critical temperature $T_c = 7.2$ K.[19] The Fermi surface of $NbSe_2$ obtained from band structure calculations[20] consists of undulating cylinders oriented along the k_z direction and centered on the H-K axis of the hexagonal Brillouin zone. However, the onset of a charge density wave at $T = 32$ K modifies its shape in certain parts of the Brillouin zone, so that the Fermi surface parameters at low temperatures are not well known. We assume, however, that the Fermi surface remains approximately cylindrical,[19,21] in which cases $m_\rho / m_z \ll 1$ and we can neglect the k_z dependence of the matrix elements (9). We chose a radial effective mass of $m_\rho = 2$, set the radius of the domain to $R = 5000$ a.u. and defined the Fermi level as

$$E_F = \frac{\hbar^2}{2m_\rho} \frac{\alpha^2_{n_F, m=0}}{R^2} \tag{16}$$

with $n_F = 120$. This results in a Fermi velocity of $v_F = 8.2 \times 10^6$ cm s^{-1}. We chose a Debye frequency of $\omega_D = 30$ meV, which, together with a coupling constant $g = 0.256$ yields a superconducting gap $\Delta_0 \simeq 1.2$ MeV at $T = 0$ in the absence of any magnetic field, and a transition temperature of $T_c \simeq 8$ K. This choice of microscopic parameters yields a coherence length and a magnetic penetration depth comparable to the experimental values, as will be shown in the next section. However, their values have not been optimized to reproduce accurately the experimental results on $NbSe_2$. Such a procedure could in principle be used to extract Fermi surface parameters from the experimentally measured ξ and λ.

III. RESULTS

The self-consistent pair potential $\Delta(r)$ calculated at temperatures ranging from 0.5 to 6 K, is shown in Fig. 1. At a temperature of 6 K, the pair potential is similar to the solution of the Ginzburg-Landau equations. As the temperature is lowered, the slope of the pair potential near $r = 0$ gets larger, indicating a drastic reduction in the size of the vortex core. At a temperature of 0.5 K, the pair potential is rising very steeply at the center of the vortex core. A coherence length ξ can be derived from these results in a variety of ways. First, we define a coherence length ξ_1 by fitting the pair potential to an expression of the form

$$\Delta(r) = \Delta_0 \tanh \frac{r}{\xi_i} . \tag{17}$$

This expression is a good approximation of the pair potential for temperatures larger than $T_c/2$. However, as can be seen from fitting Eq. (17) to the data shown in Fig. 1, it is not valid at low temperatures. We can define a second coherence length ξ_2 in another way by the relation

$$\lim_{r \to 0} \Delta(r) = \Delta_0 \frac{r}{\xi_2} . \tag{18}$$

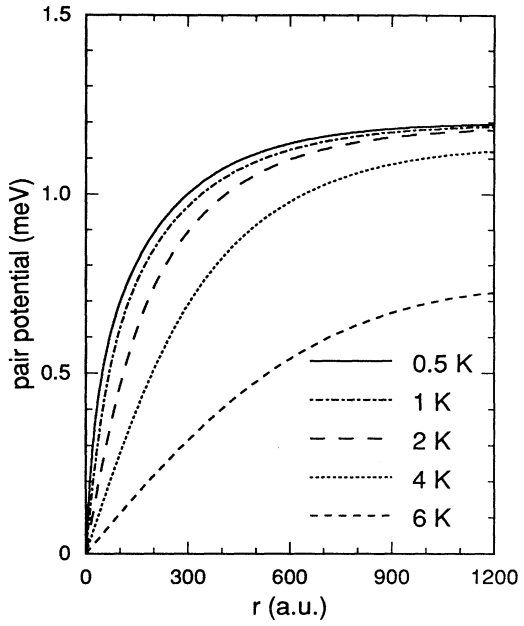

FIG. 1. Self-consistent pair potential as a function of distance from the vortex core, calculated at various temperatures.

The definitions of ξ_1 and ξ_2 agree at high temperatures where Eq. (17) is a good approximation of the pair potential. However, at low temperatures, ξ_2 becomes much smaller than ξ_1, and is ultimately comparable to the Fermi wavelength. The temperature dependence of the coherence lengths ξ_1 and ξ_2 is summarized in Fig. 2. Close to $T = T_c$, $\xi_1(T)$ and $\xi_2(T)$ can be described by an expression of the form

$$\xi(T) \propto (T_c - T)^{1/2} . \tag{19}$$

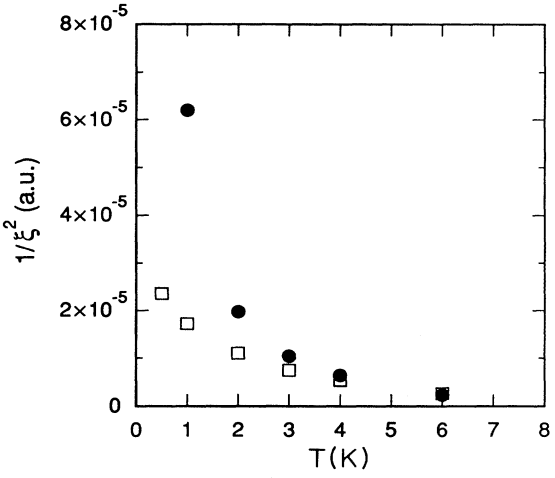

FIG. 2. Temperature dependence of $1/\xi_1^2$ (open squares) and $1/\xi_2^2$ (solid circles). At $T = 0.5$ K, $1/\xi_2^2 = 19.8 \times 10^{-5}$ a.u. (not presented).

Both ξ_1 and ξ_2 deviate significantly from this behavior at low temperatures, where, e.g., at $T=0.5$ K, $\xi_1=206$ a.u. and $\xi_2=35$ a.u. This rapid variation of the pair potential in the core at low temperatures is reminiscent of a conjecture by Kramer and Pesch,[4] who suggested that the pair potential should reach a value comparable to Δ_0 over a distance of the order of the Fermi wavelength. Their argument was based on an approximately self-consistent treatment of the pair potential close to the center of a vortex line. Our results show that the pair potential varies on *two* length scales: the first defines the slope of the pair potential at $r=0$, which becomes indeed very large as $T\rightarrow 0$, and the second a distance over which the pair potential reaches its asymptotic value Δ_0. This also indicates that the definition of the coherence length in terms of the upper critical field H_{c2}

$$\xi=\left[\frac{\phi_0}{2\pi H_{c2}}\right]^{1/2} \tag{20}$$

must be used with caution at low temperatures. Experimental measurements of the upper critical field $H_{c2}(T)$ at low temperatures[18] show that $H_{c2}(T\rightarrow 0)$ is *smaller* than the value obtained from a linear extrapolation using dH_{c2}/dT measured at T_c. The values of the coherence length ξ inferred from $H_{c2}(T)$ using Eq. (20) are therefore larger than those obtained from a linear extrapolation of $1/\xi^2(T)$ to low temperatures. However, our results (Fig. 2) show that the coherence lengths ξ_1 and ξ_2 both become *smaller* than what would be inferred from a linear extrapolation of $1/\xi^2(T)$ to low temperatures. This shows that the definition of the coherence length in terms of H_{c2} and Eq. (20) is not equivalent to either ξ_1 or ξ_2, but rather to a length which remains larger than ξ_1 and ξ_2 at low temperatures. It also shows that a certain arbitrariness is allowed in the definition of the coherence length, a fact that should be kept in mind when making quantitative comparisons with experiment. Calculations carried out at a $T=0.05$ K yield a pair density similar to that obtained at $T=0.5$ K, with additional small amplitude Friedel-like oscillations originating from the occupation of the lowest bound state.

The quasiparticle-excitation energies calculated at $T=3$ K are presented in Fig. 3 for positive values of the angular momentum μ. The eigenvalues associated with the bound states ($E<\Delta_0\simeq 1.2$ MeV) form a branch which is clearly separated from the continuum of scattering states ($E>\Delta_0$) at low angular momentum, and approaches Δ_0 asymptotically as $\mu\rightarrow\infty$. The spectrum of negative angular momentum excitations is similar, except that the branch of bound states is absent[7] (it is present for negative energies). The apparent discreteness of the spectrum above the gap ($E>\Delta_0$) in Fig. 3 results from the finite size of the domain in which we solve Eq. (1) and is artificial. In the thermodynamic limit, i.e., $R\rightarrow\infty$, the spectrum in this energy range becomes continuous. This is not true of the bound-states eigenvalues, which correspond to localized states, and are therefore insensitive to changes in the domain size. Note, however, that keeping m_ρ/m_z finite in Eq. (1) would shift the bound-state eigenvalues *upwards* by an energy of the order of k_z^2, resulting

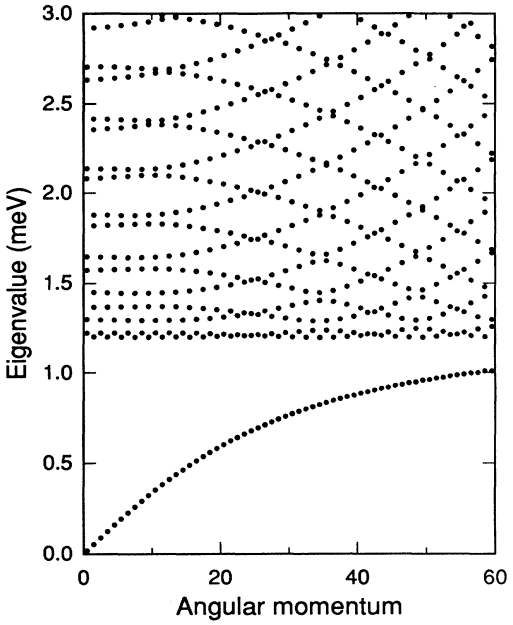

FIG. 3. Quasiparticle excitation energies for positive μ calculated at $T=3$ K.

in a continuous distribution of bound states above the lowest energy excitation $E(\mu=\frac{1}{2},k_z=0)$. This lowest eigenvalue is of the order of $\Delta_0^2/E_F=0.037$ MeV and depends on temperature. It is maximal at low temperatures as can be seen in Fig. 4. The experimental observation of this energy gap is in principle possible at temperatures lower than $T\simeq 0.5$ K. The slope $dE_\mu/d\mu$ of the dispersion relation of bound states also depends on temperature. Caroli *et al.*[6] have derived an approximate expression for this dispersion relation in terms of the coherence length,

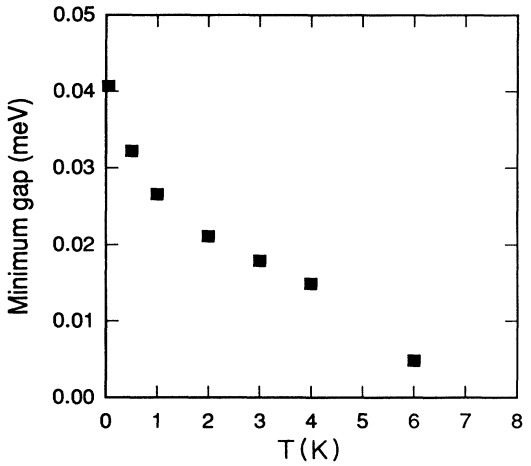

FIG. 4. Temperature dependence of the minimum energy gap $E_{1/2}$.

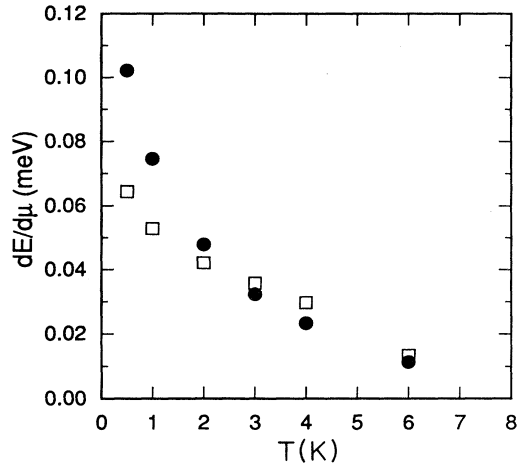

FIG. 5. Temperature dependence of $dE_\mu/d\mu$ as obtained from the self-consistent calculation (open squares) and from Eq. (21) using the coherence length ξ_1 defined by Eq. (17) (solid circles).

$$E_\mu \propto \mu \frac{\Delta_0}{k_F \xi} \simeq \mu \frac{\hbar^2}{\pi m^* \xi^2} \ . \tag{21}$$

Figure 5 shows the temperature dependence of $dE_\mu/d\mu$, as obtained from the self-consistent calculation, and compared with the value obtained by inserting $\xi_1(T)$ defined by Eq. (17), into Eq. (21). The two values coincide at temperatures larger that $T_c/2$, but deviate significantly at lower temperatures, where Eq. (21) ceases to be valid. Note that if $\xi_2(T)$ is used instead of $\xi_1(T)$ in Eq. (21), the discrepancy with the results of the self-consistent calculations at low temperatures would become even larger.

The quasiparticle amplitudes associated with low-energy eigenvalues are strongly localized in the vortex core. As an example, the radial functions $u(r)$ and $v(r)$ corresponding to the lowest eigenvalue $E_{1/2}$ are shown in Fig 6. They oscillate with a period of the order of the Fermi wavelength, and their envelope decays exponentially over a distance of the order of the coherence length. Radial functions corresponding to bound states of larger angular momenta are small close to the vortex core and have a maximum at a distance of the order of $r \simeq \mu/k_F$. Beyond that distance, their behavior is similar to that of the lowest bound state, except that their exponential decay length diverges as $E_\mu \to \Delta_0$. The quasiparticle amplitudes associated with eigenvalues larger than Δ_0 are scattering states which are extended throughout the system.

The contribution of the bound states to the total pair potential is shown in Fig. 7 where it is compared to the total pair potential for $T=0.5$ K. At low temperatures, the sharp rise of the pair potential at the vortex center is essentially due to the occupation of the lowest bound states. At larger temperatures, the contributions of bound and scattering states to the pair potential become comparable as $r \to 0$.

At large distances from the vortex core, the quasiparticles are essentially unaffected by the presence of the flux line, so that the pair potential for large r is expected to depend on temperature in the way predicted by the BCS theory of a homogeneous superconductor. This can be seen in Fig. 8, where the value of the pair potential at $r=1200$ a.u. from the vortex core is compared with the BCS prediction for a homogeneous system having the same microscopic parameters. The value obtained at $T=6$ K is slightly smaller than the BCS prediction. This is due to the fact that, at this temperature, the coherence length is large ($\xi_1 \simeq 620$ a.u.), so that the pair potential has not yet reached its asymptotic value at $r=1200$ a.u. (see Fig. 1).

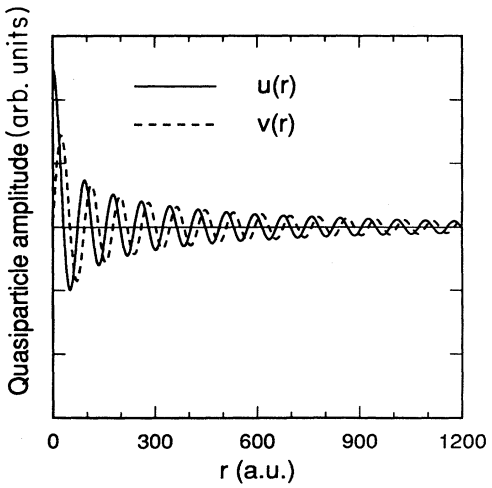

FIG. 6. Quasiparticle amplitudes $u(r)$ and $v(r)$ corresponding to the lowest eigenvalue $E_{1/2}$.

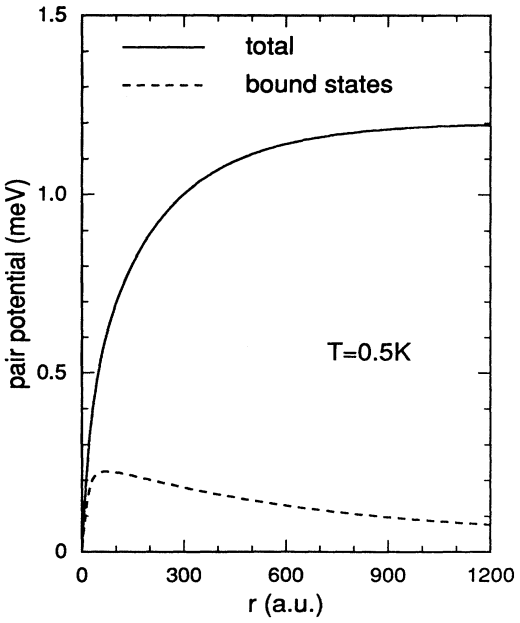

FIG. 7. Self-consistent pair potential at $T=0.5$ K. The dashed line shows the contribution from the bound states.

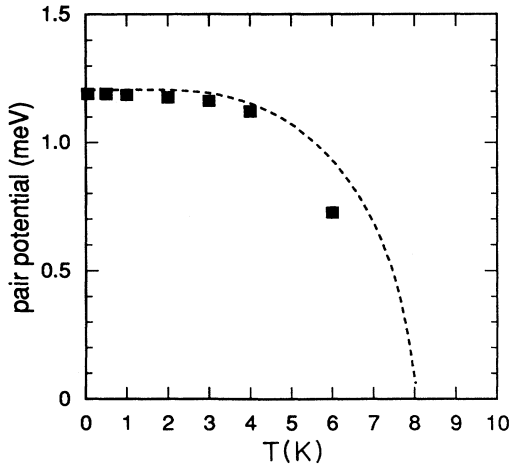

FIG. 8. Pair potential at $r=1200$ a.u. from the vortex core (solid squares), compared with the BCS prediction for a homogeneous sample (dashed line).

The self-consistent current distribution, calculated from Eq. (3) is shown in Fig. 9. At low temperatures, the current rises to its maximum over a distance of the order of ξ_2, which is consistent with the sharp rise of the pair potential in the same region. In this region, the current is mainly carried by the lowest bound state. Away from the vortex core, the current density decays exponentially. The magnetic penetration depth λ can be derived from the large r behavior of the current density by matching it at a cutoff radius $r_c=1200$ a.u. with the asymptotic solution of the Ginzburg-Landau equations[2] for large r

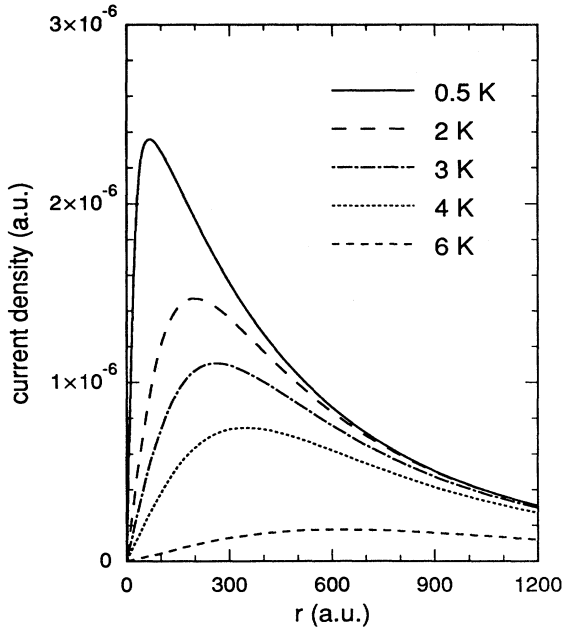

FIG. 9. Self-consistent current density calculated at various temperatures.

$$j_\theta(r)=\frac{c}{4\pi}\frac{\hbar c}{2e}\frac{1}{\lambda^3}K_1\left[\frac{r}{\lambda}\right], \tag{22}$$

where $K_1(x)$ is a modified Bessel function. The continuity of the current density at r_c, together with the flux normalization

$$\frac{4\pi}{c}\int_0^\infty \frac{r^2}{2} j_\theta(r)dr \equiv \frac{\hbar c}{2e}=\frac{\phi_0}{2\pi} \tag{23}$$

determines the value of λ. In our case, this yields a value of $\lambda=1054$ a.u. at $T=0.5$ K. The temperature dependence of the magnetic penetration depth calculated in this way is shown in Fig. 10. The linear behavior of $1/\lambda^2$ as $T\rightarrow T_c$ is consistent with the expected long wavelength response of a local homogeneous BCS superconductor.[22] The current distribution can be decomposed in terms of bound states and scattering states contributions. This is shown in Fig. 11 for a temperature of $T=4$ K. Close to the vortex core, the current density arises mainly from the occupation of the bound states. The effect of scattering states becomes important only at distances larger than the coherence length. The bound states and the scattering states contributions to the current density have *opposite signs*. The current density originating from the bound states is paramagnetic, whereas scattering states contribute a diamagnetic term. At distances larger than the penetration depth, the paramagnetic and diamagnetic parts essentially cancel, resulting in exponential decay of the total current density. The paramagnetic behavior of the bound states, which are localized in the vicinity of the core, is consistent with the picture of a vortex core behaving like a normal metal. Conversely, the scattering states are mainly located in the superconducting region $r\gg\xi$, and generate diamagnetic currents.

The magnetic field generated by the total current distribution is shown in Fig. 12 for various temperatures.

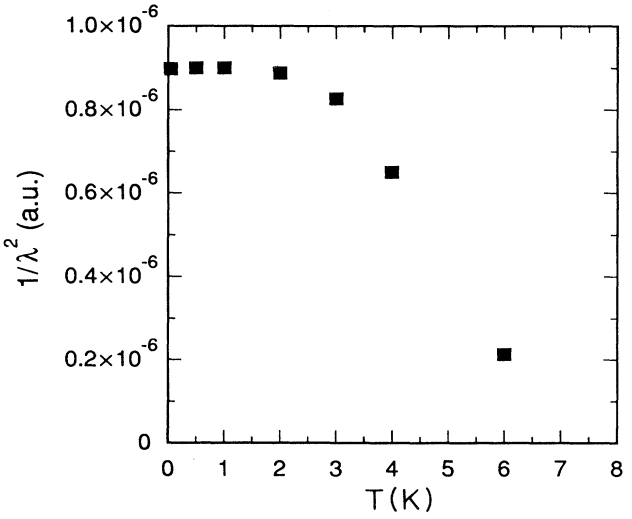

FIG. 10. Temperature dependence of $1/\lambda^2$, where λ is the magnetic penetration depth defined by Eqs. (22) and (23).

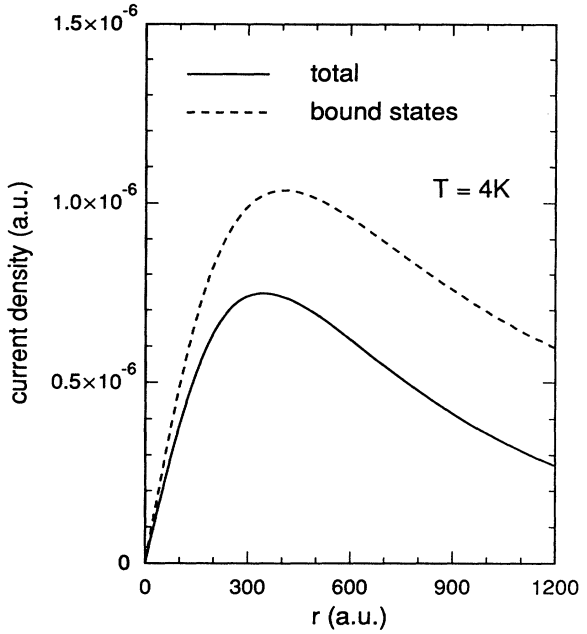

FIG. 11. Current density calculated at $T=4$ K.

The temperature dependence of the magnetic field at the center of the vortex core is shown in Fig. 13. It is approximately linear over the entire temperature range. This is to be contrasted with the prediction of the Ginzburg-Landau theory[2] (for $\kappa \gg 1$)

$$h(0)_{\mathrm{GL}}=\frac{\phi_0}{2\pi\lambda^2(T)}(\ln\kappa-0.18) \tag{24}$$

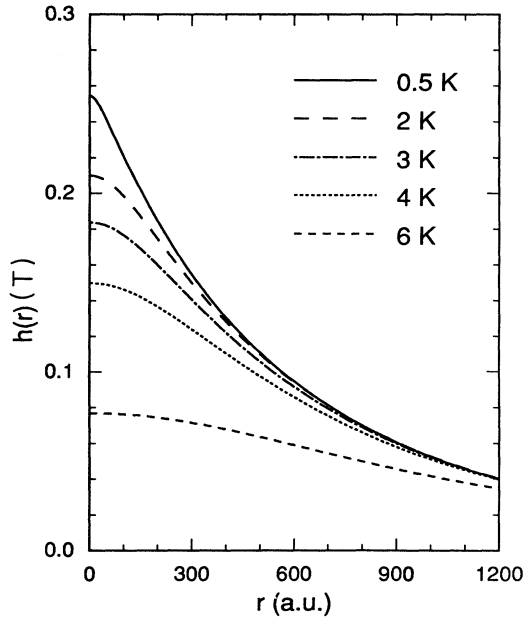

FIG. 12. Magnetic field distribution around the vortex line at various temperatures.

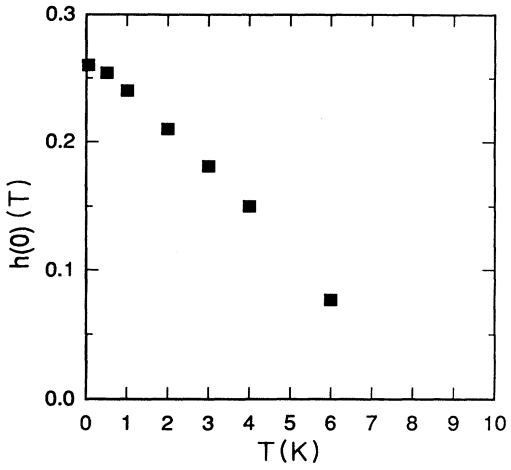

FIG. 13. Temperature dependence of the magnetic field at the center of the vortex line.

which implies that the temperature dependence of $h(0)$ should be the same as that of $1/\lambda^2$. A comparison of Figs. 13 and 10 shows that this is true only above $T_c/2$. The continuous increase of $h(0)$ below $T_c/2$ is due to the sharpening of the current distribution (see Fig 9), which is itself caused by the reduction of the core size at low temperature.

The tunneling conductance was calculated using Eq. (15) and the self-consistent quasiparticle amplitudes obtained at $T=1$ K. The conductance at various distances from the vortex center and for bias voltages ranging from -4 mV to $+4$ mV is shown in Fig. 14. It is normalized

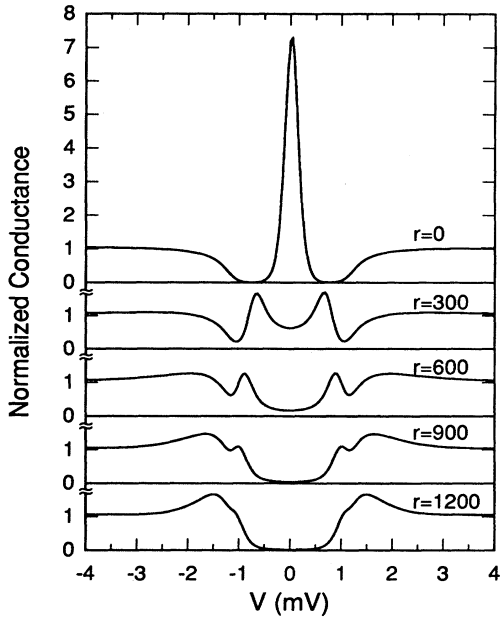

FIG. 14. Normalized tunneling conductance spectra calculated at various distances from the center of the vortex line. Distances are indicated in atomic units.

to the conductance of the normal state. At the center of the vortex core ($r=0$), the conductance is strongly enhanced at zero bias ($V=0$) due to tunneling into the $\mu=\frac{1}{2}$ lowest bound state, which is strongly localized in the core (See Fig. 6). Note that the conductance in the core is *not* enhanced around $V\simeq+\Delta_0$ as would be the case in a homogeneous superconductor. At a finite distance r from the vortex center, the conductance has two peaks[12] centered at finite voltages $\pm E_p(r)$. This corresponds to tunneling into bound states having larger angular momenta μ with eigenvalues $0<E_\mu\simeq E_p(r)<\Delta_0$ (see Fig. 3). These eigenstates have maximal amplitude at a distance of order $r\simeq\mu/k_F$ from the vortex core. This allows us to relate the position of the conductance peaks $E_p(r)$ to the dispersion relation of the bound states, which is linear for small angular momenta

$$E_\mu\simeq\mu\frac{\partial E_\mu}{\partial\mu} . \tag{25}$$

We then get the approximate relation

$$E_p(r)\simeq E_{\mu=k_F r}\simeq\frac{\partial E_\mu}{\partial\mu}k_F r, \quad r<\xi . \tag{26}$$

At temperatures larger than $T_c/2$, $\partial E_\mu/\partial\mu$ can be related to the coherence length via Eq. (21) (see Fig. 5) so that

$$E_p(r)\simeq\Delta_0\frac{r}{\xi_1(T)}, \quad T>\frac{T_c}{2} . \tag{27}$$

At low temperatures, Eq. (26) is still valid, although the simple model Eq. (21) is not applicable. In Fig. 15, the conductance calculated at $T=1$ K (left panel) is compared with the experimental conductance measured at $T\simeq0.3$ K by Hess *et al.* (right panel). Both functions show a characteristic enhancement of the zero-bias conductance due to the presence of bound states in the vortex core. The calculated value of this enhancement is larger than the experimental value, as discussed in Refs. 12 and 13. The splitting of the zero-bias conductance peak into two maxima away from the vortex core is also clearly visible in both the calculated and experimental data. The energy separation between these two maxima is $2E_p(r)$. Figure 15 shows that $E_p(r)$ increases more rapidly for the calculated function than for the experimental data. The radial dependence of $E_p(r)$ is also illustrated in Fig. 16, which represents a gray scale image of the normalized conductance as a function of bias voltage and distance from the vortex core, calculated at $T=1$ K. The availability of a direct experimental measurement of $E_p(r)$ makes it possible to adjust the microscopic parameters used in the calculation in order to reproduce this feature. The conductance enhancement due to the bound states is generally more pronounced in the calculated data than in the experimental data, even though the temperature used in the calculation is larger than the experimental temperature. This discrepancy would be reduced if a finite mass ratio m_ρ/m_z were used in Eq. (1), causing a widening of the spectral function associated with bound states. Figure 15 also shows the profile of the zero-bias conductance, which decays exponentially away from the vortex core.[6,7] This conductance profile is well represented at large r by the functional form

$$\left.\frac{\partial I(r,V)}{\partial V}\right|_{V=0}\propto\frac{1}{r}e^{-r/r_0} . \tag{28}$$

as is expected from an analysis of the asymptotic behavior of the solutions of Eq. (1). Using this expression to fit the calculated conductance yields $r_0=275$ a.u. which is comparable with the value of ξ_1 ($T=1$ K)$=240$ a.u. obtained from Eq. (17). This suggests that the length r_0 can be used as a measure of the size of the vortex core, via the degree of localization of its lowest bound states. A similar fit to the experimental data yields $r_0\simeq360$ a.u.. Because of residual noise in the measured conductance at large r, this value is only approximate.

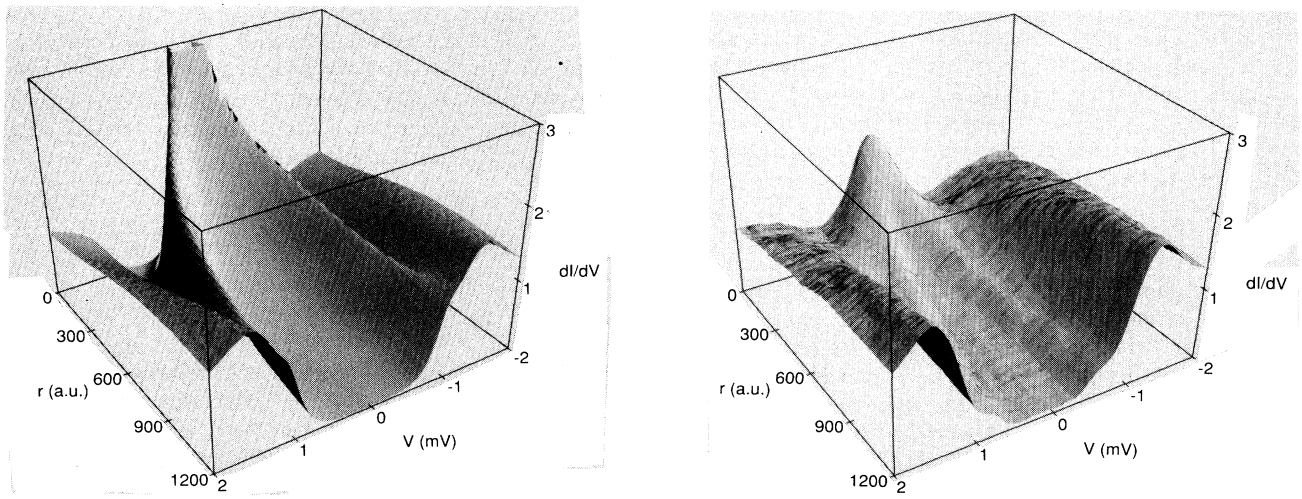

FIG. 15. Tunneling conductance represented as a function of bias voltage and distance from the vortex core, as obtained from the calculation (left panel) and from the experiment (right panel).

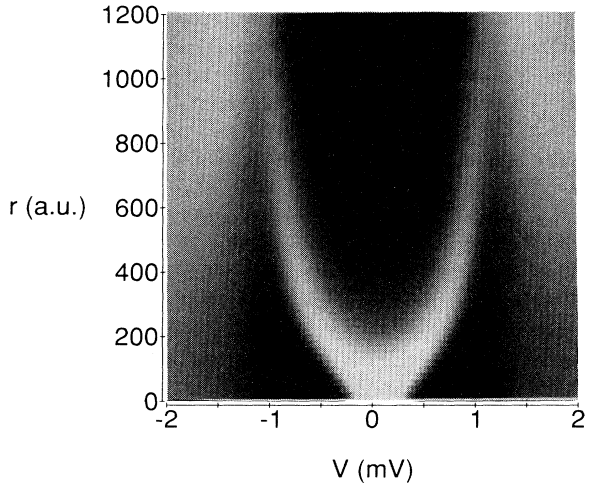

FIG. 16. Gray scale image of the tunneling conductance as a function of bias voltage and distance from the vortex core. The gray scale extends from $dI/dV=0$ (black) to $dI/dV=2$ (white).

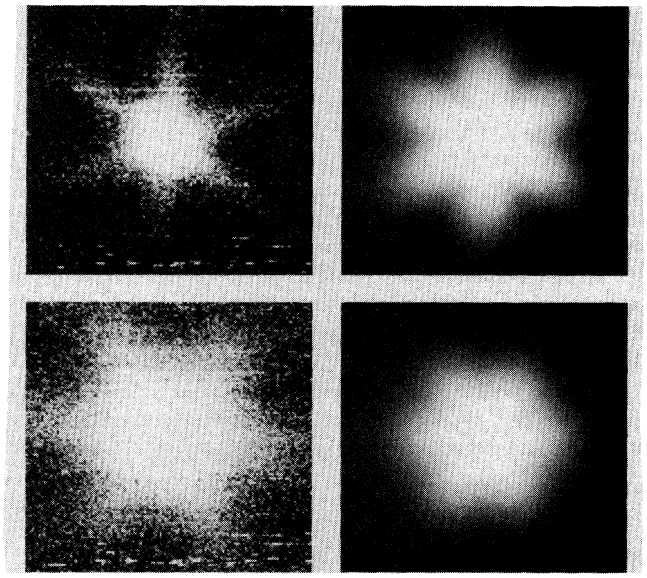

FIG. 17. Tunneling conductance images at zero bias (top row) and at finite bias (bottom row). The left column shows the experimental results of Ref. 14. Calculated images are shown in the right column. The nearest-neighbor direction of the Abrikosov flux lattice is the horizontal direction.

IV. DISTORTIONS OF A VORTEX LINE

More recent STM experiments on $NbSe_2$ carried out at very low temperatures have provided images of vortex lines in which the contours of equal tunneling conductance are not invariant under rotations about the z axis, but have instead a characteristic sixfold symmetric star shape.[16] Remarkably, the orientation of these star-shaped conductance patterns relative to the Abrikosov flux lattice was found to depend on the tunnel bias voltage. At zero bias, the measured tunneling conductance decays rapidly in the direction of the nearest-neighbor vortex lines, and more slowly in a direction 30° away from the nearest neighbors, i.e., the arms of the star pattern point towards the interstitial sites. At a bias voltage of 0.5 mV, however, the situation is reversed and the tunneling conductance decays more slowly in the direction of the nearest-neighboring vortex lines, i.e., the stars are rotated by 30° (see Fig. 17, left side). The hexagonal distortion can be caused by the presence of the neighboring flux lines, which form a triangular Abrikosov lattice, and also by the one-particle crystal potential $U(\mathbf{r})$ which, in the case of $NbSe_2$, has hexagonal symmetry. In this section, we consider the perturbation to a vortex line caused by a one-particle potential $\delta U(\mathbf{r})$ and by a vector potential $\delta\mathbf{A}(\mathbf{r})$ having a sixfold symmetry about the z axis. The one-particle potential $\delta U(\mathbf{r})$ is not pair breaking to first order, and would therefore appear to be negligible compared to the magnetic perturbation caused by $\delta\mathbf{A}$, which is pair breaking. However, since the relative magnitude of these terms is unknown, both effects are considered in the perturbation. In order to describe the changes occurring in the low-energy part of the spectrum, i.e., $E<\Delta_0$, it is sufficient to expand the Hamiltonian in the bound states calculated self-consistently in the isotropic case. The sixfold symmetry of the perturbation simplifies the problem considerably. Only bound states whose angular momentum differ by $\delta\mu=6$ are coupled by the perturbation. Including the lowest order magnetic perturbation, the diagonal blocks of the Hamiltonian in Eq. (8) become

$$T^{\pm}=\pm\left[\frac{1}{2m^*}\left[p\mp\frac{e}{c}\mathbf{A}^{(0)}\right]^2-E_F\right]-\frac{e}{2m^*c}(\delta\mathbf{A}\cdot\mathbf{p}+\mathbf{p}\cdot\delta\mathbf{A})\pm\left[\delta U(\mathbf{r})+\frac{e^2}{m^*c^2}\delta\mathbf{A}\cdot\mathbf{A}^{(0)}\right], \tag{29}$$

where $\mathbf{A}^{(0)}$ is the vector potential in the absence of perturbation. In the subspace spanned by the twelve lowest bound states, i.e., the bound states $\mu=\frac{1}{2}$ to $\mu=\frac{23}{2}$, the Hamiltonian reduces to a block diagonal matrix. Each block is a 2×2 matrix of the form

$$H_\mu=\begin{bmatrix}\langle\mu|H|\mu\rangle & \langle\mu|H|\mu+6\rangle\\ \langle\mu+6|H|\mu\rangle & \langle\mu+6|H|\mu+6\rangle\end{bmatrix}\equiv\begin{bmatrix}E_\mu^{(0)} & W_\mu\\ W_\mu & E_{\mu+6}^{(0)}\end{bmatrix}. \tag{30}$$

Note that due to the absence of rotational symmetry, the quantum number μ is not an eigenvalue of the angular momentum operator. It is now limited to values $\frac{1}{2}<\mu<\frac{11}{2}$ and labels the irreducible representations of the sixfold rotation group C_6. The eigenvalues of H_μ form two bands, labeled $+$ and $-$, which are separated by an energy gap of order $|W_{1/2}|+|W_{11/2}|$. The crossover from the lower to the upper band occurs at an energy

$$E^{(0)}_{11/2} < E_c < E^{(0)}_{13/2} \ . \tag{31}$$

The quasiparticle amplitudes, and therefore the tunneling conductance, have now lost their cylindrical symmetry. For example, in the lower band, we have

$$|u^-_\mu(\mathbf{r})|^2 = \alpha_\mu^2 |u_\mu(r)|^2 + \beta_\mu^2 |u_{\mu+6}(r)|^2 - 2\alpha_\mu\beta_\mu |u_\mu(r)||u_{\mu+6}(r)|\cos 6\theta \ . \tag{32}$$

where α_μ and β_μ are the components of the eigenvectors of H_μ. The last term in Eq. (32) introduces an angular (sixfold) modulation in the tunneling conductance, thus giving the STM images a sixfold star shape. The orientation of this star-shaped conductance pattern changes with the coefficients α_μ and β_μ which in turn depend on the value of the tunneling bias voltage. At small bias, the tunneling process occurs in the lower band whose eigenfunctions have an angular "bonding" character, whereas at a bias larger than E_c, the tunneling process involves the upper band which has "antibonding" character. The sixfold angular modulation of the conductance is therefore reversed as the bias increases from zero to above E_c, i.e., the star pattern rotates by 30°.

The *absolute* orientation of the conductance pattern is determined by the relative magnitude of the crystal potential perturbation $\delta U(\mathbf{r})$ and of the magnetic perturbation in a given direction [see Eq. (29)]. The sign of $\delta U(\mathbf{r})$ is *a priori* unknown but can in principle be obtained from detailed band structure calculations. In order to derive the sign of the magnetic perturbation, it is reasonable to assume (in the low-field limit) that the vector potential of the vortex lattice is the sum of the vector potentials of isolated vortices. The two components of the vector potential perturbation can then be approximated by

$$\delta\mathbf{A}(r,\theta) = \begin{bmatrix} \delta A_r(r)\sin 6\theta \\ \delta A^{(1)}_\theta(r) + A^{(2)}_\theta(r)\cos 6\theta \end{bmatrix} , \tag{33}$$

where $\theta = 0$ is the nearest-neighbor direction of the Abrikosov lattice. The corresponding magnetic field has maxima in the nearest-neighbor directions. Including this magnetic perturbation and neglecting $\delta U(\mathbf{r})$, we find that the resulting zero-bias star would have arms extending towards the nearest-neighbor vortices, i.e., in the directions where the magnetic field is stronger. This is consistent with the picture of the lowest bound states extending preferentially into the regions where the magnetic field is strongest, i.e., where the gap is more strongly suppressed. This is however *not* the orientation of the star observed experimentally at low field. Therefore, in the low-field limit, the crystal potential perturbation $\delta U(\mathbf{r})$ has to be dominant, so that the total perturbation is repulsive in the nearest-neighbor direction and attractive in the interstitial direction. In other words, the orientation of the stars in $NbSe_2$ seems to be determined by the underlying crystal potential and not by the Abrikosov flux lattice. This competition between the effect of the magnetic field and the crystal potential suggests that this situation might be reversed in high magnetic fields. The magnitude of the matrix elements of the magnetic perturbation also depends on μ. At large μ and not too small fields, the increasing magnetic perturbation may cause the matrix element W_μ to change sign, which would result in an additional distortion of the star-shaped pattern at large distances from the core, where the contributions to the conductance from states with large μ become important. In such a case, the arms of the zero-bias stars would be oriented along the interstitial directions close to the vortex cores, and along the nearest-neighbor directions away from the vortex core.

The tunneling conductance in the presence of a hexagonal perturbation was calculated as a function of distance from the vortex core, assuming a value of $|W_\mu|/\Delta_0 = 0.05$, independent of μ. This value is comparable to the energy spacing between the lowest quasiparticle bound states of the isolated vortex. The resulting modified spectrum is shown in Fig. 18, together with the unperturbed spectrum. Conductance profiles calculated in the direction of the nearest-neighboring vortex and in the interstitial direction are shown in Fig. 19 at both zero bias and a bias of $\Delta_0/5$, which corresponds to the bottom of the lower and of the upper bands, respectively (see Fig. 18). The experimental curves of Ref. 16 are also shown in Fig. 19 for comparison. The two-band model correctly predicts the reversal of the anisotropy of the tunneling conductance between low- and high-bias voltage, as can be seen by comparing solid and dashed lines. The calculated conductance $\partial I(r,\theta,V)/\partial V$ was used to produce a gray scale image, similar to the experiment image of Ref. 16. It is compared to experiment in Fig. 17 (right column). The shape of the zero-bias star observed experimentally is somewhat different from the calculated one. This indicates that the angular modulation of the conductance has more structure than is described by the last term in Eq. (32). The inclusion of more bound states in

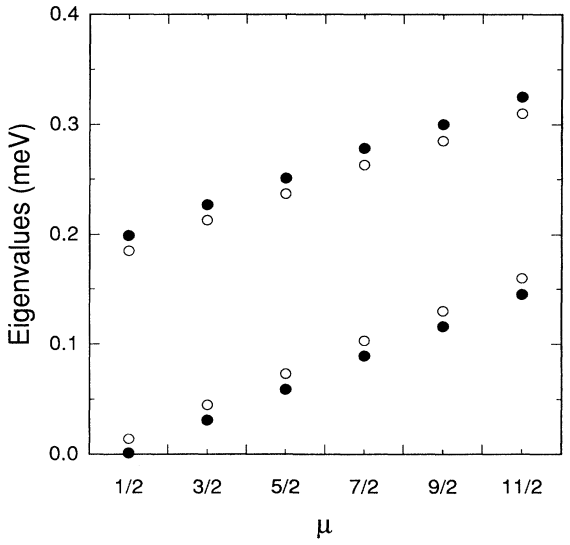

FIG. 18. Low-energy part of the quasiparticle spectrum, of a vortex line in the cylindrically symmetric case (open circles) and in the presence of a sixfold symmetric perturbation (solid circles). The spectrum is Bragg reflected at the first Brillouin-zone boundary $\mu = 6$.

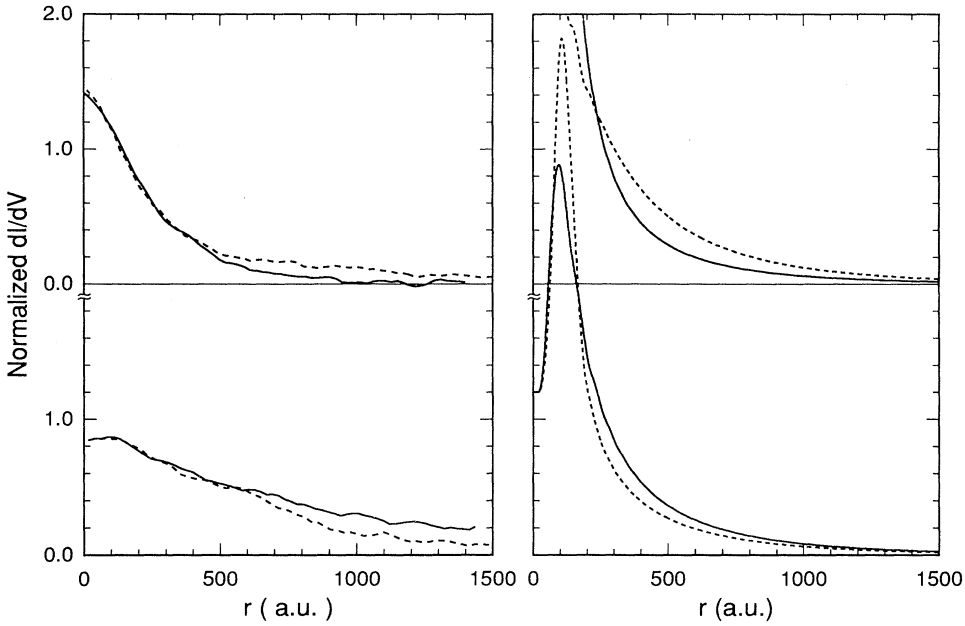

FIG. 19. Tunneling differential conductance profiles calculated at zero bias (top right) and at a finite bias of $V=\Delta_0/5$ (bottom right) in the direction of the nearest-neighboring flux line (solid lines) and in the interstitial direction (dashed lines). The experimental results from Ref. 14 are shown in the left panels.

the treatment of the perturbation would result in a more accurate description of the conductance.

V. CONCLUSIONS

Self-consistent solutions of the microscopic Bogoliubov–de Gennes equations provide new insights into the properties of quasiparticles in the vicinity of a vortex line. Various properties can be studied at low temperatures, where the validity of the Ginzburg-Landau theory is limited. The self-consistent solutions show a strong reduction in the size of the vortex core at low temperatures, exhibiting variations of the pair potential over *two* length scales: the Fermi wavelength and the traditional coherence length. Spatially resolved excitation spectra measured in an STM experiment can also be understood using simple models of the tunneling current. In particular, the modifications of the conductance due to the presence of bound states in the vortex core are well reproduced within the Bogoliubov–de Gennes formalism. Comparison of the calculated conductance profiles with the experimental results allows one to determine microscopic parameters of the Fermi surface in the normal state. Finally, spatial distortions of a vortex line are studied by including additional terms to the Bogoliubov–de Gennes Hamiltonian in perturbation theory. For instance, it is found that perturbations due to the underlying crystal potential deform the vortex into a starlike pattern. This has been observed in STM experiments. Extensions of this work to a self-consistent calculation of the properties of a periodic flux lattice would be needed in order to investigate the properties of quasiparticles in a magnetic field close to the upper critical field H_{c2}. A calculation of the electronic properties of an isolated magnetic impurity in a superconductor would also be of interest, since this situation can in principle be investigated in an STM experiment.

ACKNOWLEDGMENTS

We would like to thank H. Hess and T. Palstra for many fruitful discussions. One of us (F.G.) acknowledges financial support from the Swiss National Science Foundation.

*Present address: IBM Research Division, CH-8803 Rüschlikon, Switzerland.

[1]For a review, see N. R. Werthamer, in *Superconductivity*, edited by R. D. Parks (Marcel Dekker, New York, 1969).

[2]For a review, see A. L. Fetter and P. C. Hohenberg, in *Superconductivity* (Ref. 1).

[3]G. Eilenberger, Z. Phys. **214**, 195 (1968).

[4]L. Kramer and W. Pesch, Z. Phys. **269**, 59 (1974).

[5]U. Klein, Phys. Rev. B **40**, 6601 (1989).

[6]C. Caroli, P. G. de Gennes, and J. Matricon, Phys. Lett. **9**, 307 (1964); C. Caroli and J. Matricon, Phys. Kondens. Mater. **3**, 380 (1965); C. Caroli, Ann. Inst. Henri Poincaré A **4**, 159 (1966).

[7]J. Bardeen, R. Kümmel, A. E. Jacobs, and L. Tewordt, Phys. Rev. **187**, 556 (1969).

[8]A. R. Bishop, P. S. Lomdahl, J. R. Schrieffer, and S. A. Trugman, Phys. Rev. Lett. **61**, 2709 (1988).

[9]L. P. Gor'kov, Zh. Eksp. Teor. Fiz. **36**, 1918 (1959) [Sov. Phys.

JETP **9**, 1364 (1959)]. See also V. Ambegaokar, in *Superconductivity* (Ref. 1).

[10]See, e.g., P. G. de Gennes, *Superconductivity of Metals and Alloys* (Addison-Wesley, Reading, MA, 1989).

[11]A. L. Fetter and J. D. Walecka, *Quantum Theory of Many-particle Systems* (McGraw-Hill, New York, 1971).

[12]J. D. Shore, M. Huang, A. T. Dorsey, and J. P. Sethna, Phys. Rev. Lett. **62**, 3089 (1989)

[13]F. Gygi and M. Schlüter, Phys. Rev. B **41**, 822 (1990).

[14]H. Hess, R. B. Robinson, R. C. Dynes, J. M. Valles, Jr., and J. V. Waszczak, Phys. Rev. Lett. **62**, 214 (1989); J. Vac. Sci. Technol. A **8**, 450 (1990).

[15]F. Gygi and M. Schlüter, Phys. Rev. Lett. **65**, 1820 (1990).

[16]H. Hess, R. B. Robinson, and J. V. Waszczak, Phys. Rev. Lett. **64**, 2711 (1990).

[17]See, e.g., G. D. Mahan, *Many-Particle Physics* (Plenum, New York, 1981).

[18]P. de Trey, S. Gygax, and J. P. Jan, J. Low Temp. Phys. **11**, 421 (1973); B. W. Pfalzgraf and H. Spreckels, J. Phys. C **27**, 4359 (1987).

[19]J. E. Graebner and M. Robbins, Phys. Rev. Lett. **36**, 422 (1976).

[20]L. F. Mattheiss, Phys. Rev. Lett. **30**, 784 (1973); Phys. Rev. B **8**, 3719 (1973).

[21]J. A. Wilson, Phys. Rev. B **15**, 5748 (1977).

[22]B. Mühlschlegel, Z. Phys. **155**, 313 (1959); see also Ref. 11, p. 460.

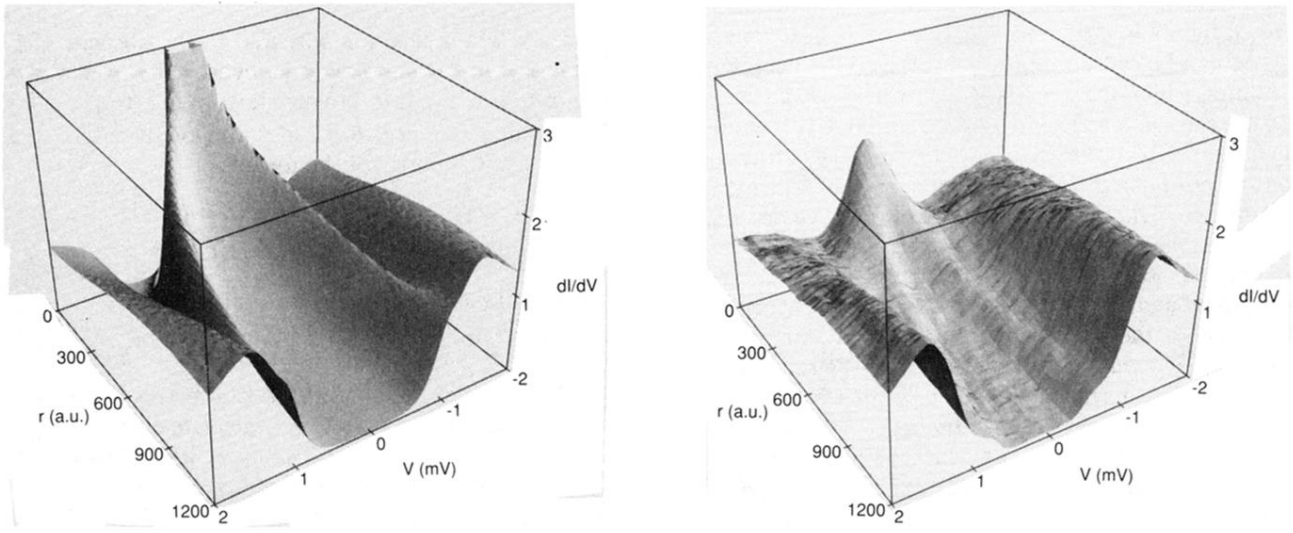

FIG. 15. Tunneling conductance represented as a function of bias voltage and distance from the vortex core, as obtained from the calculation (left panel) and from the experiment (right panel).

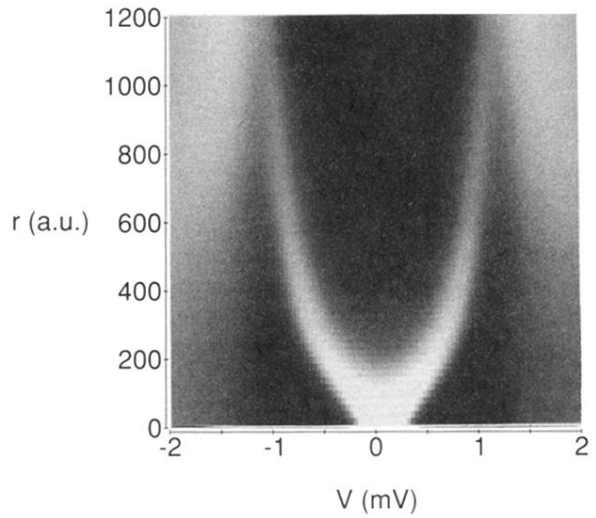

FIG. 16. Gray scale image of the tunneling conductance as a function of bias voltage and distance from the vortex core. The gray scale extends from $dI/dV=0$ (black) to $dI/dV=2$ (white).

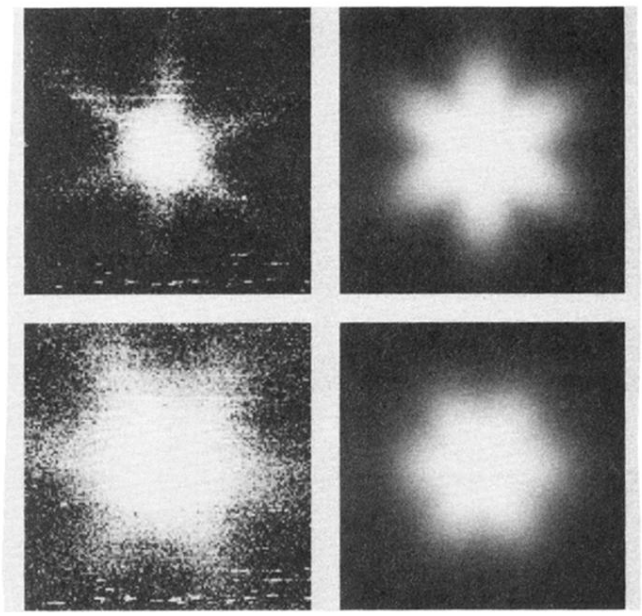

FIG. 17. Tunneling conductance images at zero bias (top row) and at finite bias (bottom row). The left column shows the experimental results of Ref. 14. Calculated images are shown in the right column. The nearest-neighbor direction of the Abrikosov flux lattice is the horizontal direction.